Improved Adaptive Sliding-Mode Observer Based Position Sensorless Control for Variable Flux Memory Machines

Yuxiang Zhong, Heyun Lin, *Senior Member, IEEE*, Jiyao Wang, *Member, IEEE*,
and Hui Yang, *Senior Member, IEEE*

***Abstract*—This article focuses on the position sensorless control for variable flux memory machine (VFMM) of which the magnetization state (MS) can be flexibly changed by applying a *d*-axis current pulse to achieve the so-called MS manipulation. First, the unique challenges in VFMM sensorless control are in depth analyzed and summarized based on the experimental results. An improved adaptive sliding-mode observer (SMO) and an improved phase-locked loop (PLL) are then proposed. Specifically, a newly developed *dq*-axis voltage pulse injection method is employed to accurately measure the *dq*-axis inductances of VFMM during MS manipulations and update them into SMO to increase its convergence speed. An adaptive law is proposed for tuning sliding-mode gains to obtain satisfying estimation performance of SMO under different conditions of speed and MS. In addition, to enhance the position tracking performance against the position estimation error resulted from MS manipulation or speed change, an improved PLL is structured, whose bandwidth can be adaptively adjusted by using fuzzy logic control. Finally, the feasibility and effectiveness of the proposed sensorless control strategy are verified through experimental measurements on a hybrid magnetic circuit VFMM prototype.**

***Index Terms*—Adaptive sliding-mode observer (SMO), fuzzy logic control, magnetization state (MS) manipulation, sensorless control, variable flux memory machines (VFMMs).**

I. INTRODUCTION

VARIABLE flux memory machine (VFMM), a type of permanent magnet synchronous machine (PMSM), has been recognized as a wide-speed machine in the true sense since its air-gap flux can be flexibly adjusted by changing the magnetization states (MSs) of the equipped low coercive force permanent magnets (PMs) with short *d*-axis current pulses [1], [2], [3], [4], [5], [6], [7], [8], [9], [10], [11]. With properly selected MSs, VFMM can achieve wider speed operation while maintaining higher overall efficiency compared with the traditional PMSM. Commonly, a high MS is desired in the constant torque low-speed region to produce large torque, while a low MS is preferred in the constant power region to extend the speed range by reducing the required flux weakening *d*-axis current. Therefore, VFMM exhibits significant feasibility for wide speed range operations, which are required for many applications, such as electric vehicles, high-speed machine tools, and flywheel energy storage [6], [7].

In most drive systems for the traditional PMSMs, position sensors are mechanically mounted on rotor shafts to obtain the rotor angles. The system volume, cost, and maintenance requirements can be further reduced when the position sensor is saved. Moreover, the sensors are vulnerable to electromagnetic noise in harsh conditions and have a limited operating-temperature range, reducing the system reliability. To avoid these drawbacks, various position sensorless control methods have been extensively investigated for PMSMs. These existing methods [12], [13], [14], [15], [16], [17], [18], [19], [20], [21], [22], [23], [24], [25], [26], [27], [28], [29], [30], [31], [32], [33] can be divided into two categories, namely signal injection method [13], [14] and back electromotive force (EMF) based method [15], [16], [17], [18], [19], [20], [21], [22], [23], [24], [25], [26], [27], [28], [29], [30], [31], [32], [33] used in zero/low-speed range and middle/high-speed range, respectively. Back EMF based methods can be roughly categorized as flux observer [16], [17], full/reduced-order state observer [18], [19], [20], model reference adaptive system [21], extended Kalman filter [22], [23], and sliding-mode observer (SMO) [24], [25], [26], [27], [28], [29], [30], [31], [32], [33] estimation methods. Compared with other methods, SMO has simpler structure, stronger robustness, and lower sensitivity to parameter variation, which has been extensively applied to sensorless controls of PMSMs.

An adaptive SMO strategy is developed in [25] for the wide speed operation of surface PMSM in which the observer gains are dynamically adjusted according to the estimated back EMFs. In [26], a new integral sliding-mode function with variable

Manuscript received 22 August 2022; revised 15 December 2022; accepted 6 January 2023. Date of publication 9 January 2023; date of current version 10 March 2023. This work was supported in part by the National Natural Science Foundation of China under Grants 52037002 and 52077033, in part by the Key R&D Program of Jiangsu Province (No. BE2021052), in part by "Thousand Talents Plan" Project of Jiangxi Province (No. jxsq2020102088), in part by the GF Key Laboratory of Science and Technology Foundation Project under Grant 6142217210201, and in part by the "Postgraduate Research and Practice Innovation Program of Jiangsu Province" (No. KYCX22_0256). Recommended for publication by Associate Editor K.-B. Lee. *(Corresponding author: Heyun Lin.)*

The authors are with the School of Electrical Engineering and Suzhou Institute, Southeast University, Nanjing 210096, China (e-mail: seu_emat_zhongyx@163.com; hyling@seu.edu.cn; jyaowang@seu.edu.cn; huiyang@seu.edu.cn).

Color versions of one or more figures in this article are available at https://doi.org/10.1109/TPEL.2023.3235594.

Digital Object Identifier 10.1109/TPEL.2023.3235594

boundary layer function is presented to suppress the chattering and accelerate the convergence speed of the system. In [27], the advantages and drawbacks of the sign and sigmoid functions are analyzed in detail, and the phase lag when using sigmoid function is well compensated. A supertwisting SMO with adaptive gains is proposed in [28] to reduce the chattering without low-pass filters and achieve the accurate position estimation in a wide speed range. An adaptive supertwisting SMO considering voltage-source-inverter nonlinearity is proposed in [29] in which the sliding-mode gains are tuned online by an adaptive algorithm and the distorted voltages are online estimated and compensated. In [30], a fuzzy logic control method is used to adaptively adjust sliding-mode gains to maintain good performance under different operating conditions.

Unfortunately, the investigation on sensorless control of VFMMs has not been reported so far. It is facing several new challenges since this kind of machine has the unique MS manipulations using large d-axis current pulses compared with the traditional PMSMs. The large position estimation error induced by MS manipulation could cause fatal impacts on the VFMM drive system, including not only MS manipulation failure, i.e., the machine fails to be magnetized or demagnetized to the desired MS, but also undesirable speed fluctuations that degrade the stability of drive system. Studying the sensorless control can fundamentally avoid the drawbacks of position sensors and improve the robustness of the VFMM drive system, further extending its application. Besides, it can also provide some valuable experience for PMSM sensorless control against the short-duration large currents circumstances.

This article aims to study the position sensorless control strategy for VFMMs. First, the challenges in VFMM sensorless control are identified and analyzed based on the experimental results of VFMM in detail. Then, an improved adaptive SMO and an improved phase-locked loop (PLL) are proposed to guarantee the position estimation accuracy at different MSs as well as during the short transitions of MS manipulations. Specifically, the dq-axis inductances during MS manipulations are measured in advance through a newly developed dq-axis voltage pulse injection method and embedded in SMO to achieve a better convergence speed. An adaptive law is proposed for tuning the sliding-mode gains based on both MS and speed to obtain good performance over a wide speed range. An improved PLL is structured, which adopts fuzzy logic control to tune the bandwidth for better position tracking performance during MS manipulation. Finally, a position sensorless control system for VFMM is developed to verify the proposed control strategy. The main original work can be concisely summarized as follows.

1) The challenges of VFMM sensorless control are clearly identified for the first time.
2) An improved dq-axis voltage pulse injection method is proposed to measure the dq-axis inductances considering the MS change.
3) An adaptive law of sliding-mode gains is constructed considering both MS and speed, and the current errors are also utilized to regulate the gains during MS manipulations.
4) A fuzzy logic control-based PLL with variable bandwidth is proposed for better position tracking.

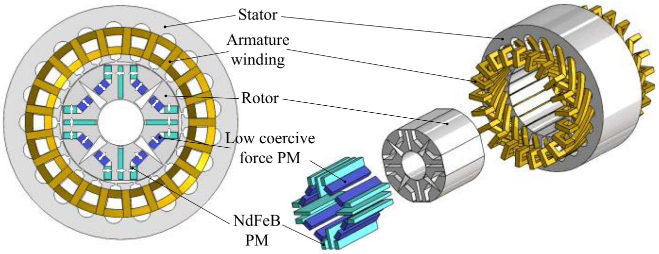

Fig. 1. Topology of investigated HMC-VFMM [2].

The rest of this article is organized as follows. In Section II, the topology and MS manipulation characteristics of the investigated hybrid magnetic circuit VFMM (HMC-VFMM) are demonstrated. In Section III, the conventional sensorless control based on SMO is briefly introduced. Then, the challenges in VFMM sensorless control are analyzed and summarized based on the experimental results using the conventional SMO. In Section IV, the proposed sensorless control strategy for VFMM is elaborated and demonstrated in detail. The feasibility and effectiveness of the proposed sensorless control strategy are validated through experiments on the HMC-VFMM prototype in Section V. Finally, Section VI concludes this article.

II. MACHINE TOPOLOGY AND MS MANIPULATION CHARACTERISTICS

A. Machine Topology

The topology of the studied HMC-VFMM [2] is depicted in Fig. 1, which combines the advantages of parallel and series magnetic circuits. The parallel branch can short circuit the majority of high coercive force PM magnetic fluxes within the rotor core when the low coercive force PMs are demagnetized, thus increasing the flux regulation range. On the other hand, the series magnetic circuit can remarkably improve the on-load demagnetization withstand capability with the help of the triangular q-axis barriers. The MS of the low coercive force PMs can be flexibly changed by applying d-axis current pulses, extending the speed range of the machine consequently.

B. MS Manipulation Characteristics

Fig. 2 depicts a simplified hysteresis model of low coercive force PM to illustrate the flux regulation principle of VFMM. The initial operating point of low coercive force PM is assumed as B_{r1}, corresponding to a high MS. When a negative d-axis current pulse is applied to demagnetize the PM, the operating point is driven to move across the knee point and down to a new state B_{r2}. If the d-axis current becomes sufficiently negative, the magnetization direction of low coercive force PM will be reversed, and the operating point can settle at a negative level B_{r3}. Similarly, when applying a positive d-axis current pulse, the operating point of low coercive force PM at B_{r2} or B_{r3} can recover to B_{r1}, denoted by the red arrows. Therefore, the PM flux linkage of VFMM can be flexibly changed by adjusting the MS of low coercive force PM.

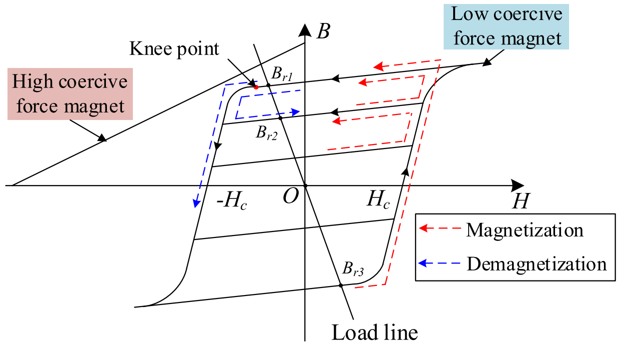

Fig. 2. Simplified hysteresis model of low coercive force PM.

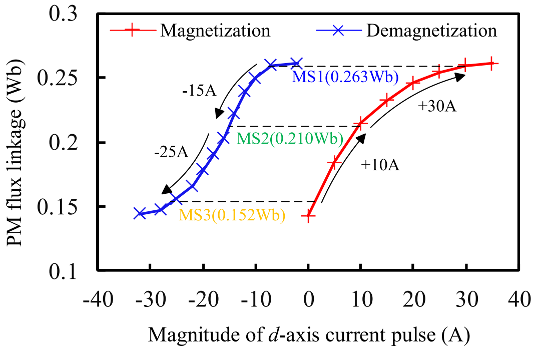

Fig. 3. Relationship between the PM flux linkage and the magnitude of *d*-axis current pulse of the HMC-VFMM [2].

Fig. 3 shows the relationship between the PM flux linkage and the magnitude of *d*-axis current pulse of the studied HMC-VFMM. Frequent magnetization and demagnetization of the low coercive force PMs will inevitably produce large pulsating torques accompanied by mechanical vibrations and noises. Therefore, in practice, three specific MSs, i.e., MS1 (the highest), MS2 (the intermediate), and MS3 (the lowest), are selected to simplify the MS manipulation and maintain an operation region almost the same as if the MS was adjusted continuously. The required *d*-axis current pulses corresponding to four MS manipulations are also denoted in Fig. 3 to clearly show the MS characteristics of the studied prototype. It should be noted that the sensorless control strategy investigated in this article is also applicable to other VFMM topologies as they have the same MS manipulation characteristics.

III. ANALYSIS OF SENSORLESS CONTROL FOR VFMM

A. Mathematical Model of VFMM

The voltage equation and the electromagnetic torque of VFMM in the *d*–*q* reference frame can be written as follows:

$$\begin{cases} u_d = Ri_d + L_d\frac{di_d}{dt} + \frac{d\psi_{\mathrm{PM}}(i_d)}{dt} - \omega_e L_q i_q \\ u_q = Ri_q + L_q\frac{di_q}{dt} + \omega_e L_d i_d + \omega_e \psi_{\mathrm{PM}}(i_d) \end{cases} \tag{1}$$

$$T_e = \frac{3}{2}p[\psi_{\mathrm{PM}}(i_d)i_q + (L_d - L_q)i_d i_q] \tag{2}$$

where u_d and u_q are the *dq*-axis voltages, i_d and i_q are the *dq*-axis currents, R is the phase resistance, L_d and L_q are the *dq*-axis inductances, ω_e is the rotor electrical angular speed, p is the number of pole pairs, and $\psi_{\mathrm{PM}}(i_d)$ is the variable PM flux linkage, which is determined by the magnitude of *d*-axis current pulse. The term $d\psi_{\mathrm{PM}}(i_d)/dt$ is approximately equal to zero under normal operations at a fixed MS; however, it cannot be neglected during MS manipulations due to the changes of PM flux linkage, which is obviously different from PMSM.

B. Conventional Sensorless Control Based on SMO

According to the mathematical model of PMSM, the current equation in the $\alpha\beta$ stationary reference frame can be expressed as follows [13]:

$$\frac{d}{dt}\begin{bmatrix} i_\alpha \\ i_\beta \end{bmatrix} = \boldsymbol{A}\begin{bmatrix} i_\alpha \\ i_\beta \end{bmatrix} + \frac{1}{L_d}\begin{bmatrix} u_\alpha \\ u_\beta \end{bmatrix} - \frac{1}{L_d}\begin{bmatrix} e_\alpha \\ e_\beta \end{bmatrix} \tag{3}$$

where the matrix $\boldsymbol{A}$ can be written as follows:

$$\boldsymbol{A} = \frac{1}{L_d}\begin{bmatrix} -R & -\omega_e(L_d - L_q) \\ \omega_e(L_d - L_q) & -R \end{bmatrix} \tag{4}$$

and i_α and i_β are the $\alpha\beta$-axis currents, u_α and u_β are the $\alpha\beta$-axis voltages, and e_α and e_β are the $\alpha\beta$-axis extended EMFs, respectively.

To estimate the extended EMFs, the current observer based on the conventional SMO is expressed as follows:

$$\frac{d}{dt}\begin{bmatrix} \hat{i}_\alpha \\ \hat{i}_\beta \end{bmatrix} = \boldsymbol{A}\begin{bmatrix} \hat{i}_\alpha \\ \hat{i}_\beta \end{bmatrix} + \frac{1}{L_d}\begin{bmatrix} u_\alpha \\ u_\beta \end{bmatrix} - \frac{1}{L_d}\begin{bmatrix} v_\alpha \\ v_\beta \end{bmatrix} \tag{5}$$

where $\hat{i}_\alpha$ and $\hat{i}_\beta$ are the observed values of the $\alpha\beta$-axis currents, and v_α and v_β are the equivalent $\alpha\beta$-axis sliding-mode functions.

Thus, the current errors can be obtained by subtracting (3) from (5), as follows:

$$\frac{d}{dt}\begin{bmatrix} \tilde{i}_\alpha \\ \tilde{i}_\beta \end{bmatrix} = \boldsymbol{A}\begin{bmatrix} \tilde{i}_\alpha \\ \tilde{i}_\beta \end{bmatrix} + \frac{1}{L_d}\begin{bmatrix} e_\alpha - v_\alpha \\ e_\beta - v_\beta \end{bmatrix} \tag{6}$$

where $\tilde{i}_\alpha = \hat{i}_\alpha - i_\alpha$ and $\tilde{i}_\beta = \hat{i}_\beta - i_\beta$ are the $\alpha\beta$-axis current errors.

The sliding-mode control law is usually designed as follows:

$$\begin{bmatrix} v_\alpha \\ v_\beta \end{bmatrix} = \begin{bmatrix} kf\left(\hat{i}_\alpha - i_\alpha\right) \\ kf\left(\hat{i}_\beta - i_\beta\right) \end{bmatrix} \tag{7}$$

where k is the sliding-mode control gain, and $f(\cdot)$ is the switching function, such as traditional symbolic function "sign(·)."

When the state variables reach the sliding surfaces, namely $\tilde{i}_\alpha = 0$ and $\tilde{i}_\beta = 0$, they will keep moving around the sliding surfaces so that it can be obtained as follows:

$$\begin{bmatrix} e_\alpha \\ e_\beta \end{bmatrix} = \begin{bmatrix} v_\alpha \\ v_\beta \end{bmatrix} = \begin{bmatrix} kf\left(\hat{i}_\alpha - i_\alpha\right) \\ kf\left(\hat{i}_\beta - i_\beta\right) \end{bmatrix}. \tag{8}$$

Since v_α and v_β contain high-frequency switching signals, low-pass filters are usually employed to extract the $\alpha\beta$-axis estimated extended EMFs, $\hat{e}_\alpha$ and $\hat{e}_\beta$, which will be further used to estimate the position and speed.

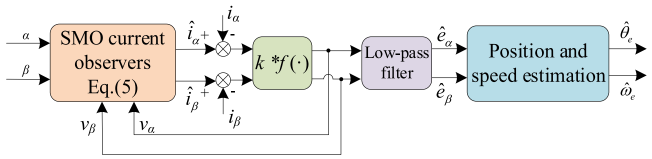

Fig. 4. Schematic diagram of the sensorless control based on SMO.

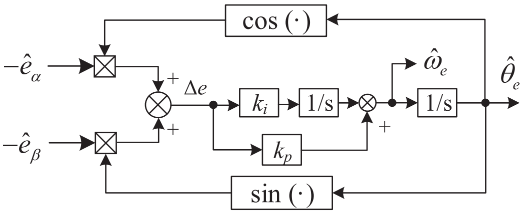

Fig. 5. Structure of the typical PLL.

The schematic diagram of the conventional sensorless control based on SMO is shown in Fig. 4. The position and speed estimation can be implemented by using a PLL, which outperforms the method using an arctangent function in mitigating the influence of noise and harmonics. The structure of the typical PLL is shown in Fig. 5.

The extended EMF error Δe is defined as follows:

$$\begin{aligned}\Delta e &= -\hat{e}_\alpha \cos\hat{\theta}_e - \hat{e}_\beta \sin\hat{\theta}_e \\ &= -E_{\rm ex}\sin(\hat{\theta}_e - \theta_e) \approx -E_{\rm ex}(\hat{\theta}_e - \theta_e) = -E_{\rm ex}\Delta\theta_e\end{aligned} \tag{9}$$

where $E_{\rm ex} = (L_d - L_q)(\hat{\omega}_e i_d - di_q/dt) + \hat{\omega}_e \psi_{\rm PM}$ is the amplitude of the extended EMF, θ_e and $\hat{\theta}e$ are the rotor position and its estimated value, respectively, and $\Delta\theta_e$ is the position estimation error. The transfer function of the PLL can be expressed as follows:

$$G_{\rm PLL} = \frac{\hat{\theta}_e}{\theta_e} = \frac{E_{\rm ex}k_p s + E_{\rm ex}k_i}{s^2 + E_{\rm ex}k_p s + E_{\rm ex}k_i} \tag{10}$$

where k_p and k_i are the proportional and integration gains of the PI regulator, respectively.

C. Challenges in VFMM Sensorless Control

Since the PM flux linkage of VFMM is adjusted by injecting the d-axis current pulses with large amplitudes, some unique problems occur for the drive system of this kind of machine when applying conventional sensorless control methods.

1) Parameter Designs of Observers and PLL at Different MSs: It is well known that the observer with a constant sliding-mode control gain k cannot achieve good performance over a wide speed range for PMSM, even though the PM flux linkage is constant. Commonly, a large value of k is required to guarantee the stability of SMO at high speed operation, while a large gain will cause chattering at low-speed operation. This is due to the variations of back EMF at different speeds. Similarly, the performance of PLL with constant parameters will also be affected by the speed variation. For VFMM, the back EMF changes with MS besides speed, further increasing the difficulty in the parameter designs of SMO and PLL.

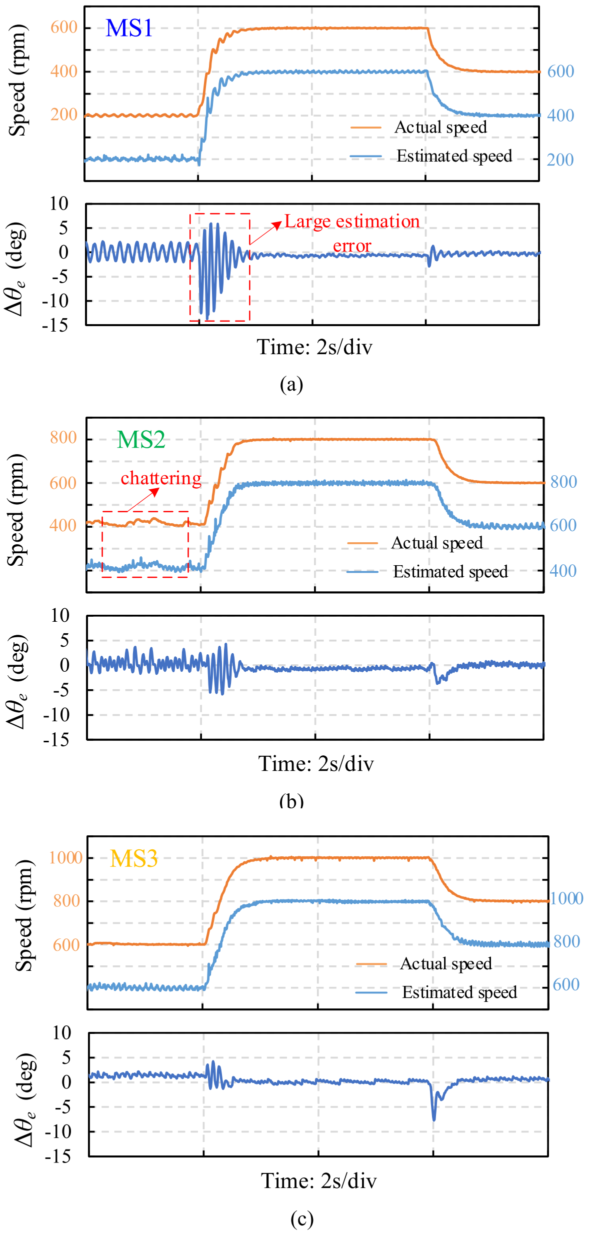

(a)

(b)

(c)

Fig. 6. Experimental waveforms of speed and position estimation errors by using the conventional sensorless control based on SMO with constant parameters, at the three MSs. (a) At MS1. (b) At MS2. (c) At MS3.

Fig. 6 shows the experimental waveforms of speed and position estimation errors at the three MSs by using the conventional SMO with constant parameters, under both the acceleration and deceleration operations. It can be clearly observed that the position estimation at MS3 exhibits small errors at steady state, acceleration, and deceleration. For the other two cases, the position estimation error increases when the speed accelerates from 200 to 600 r/min at MS1, and a speed chattering occurs at 400 r/min at MS2. The back EMFs are different at these cases due to the different MS and speed, causing that the initial conditions of the state variables are different. The good

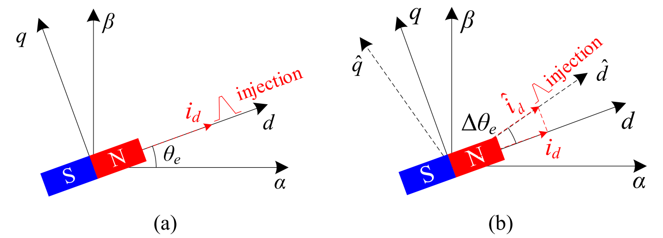

(a) (b)

Fig. 7. MS manipulations with the *d*-axis current pulses at two different rotor reference frames. (a) Actual reference frame. (b) Estimated reference frame.

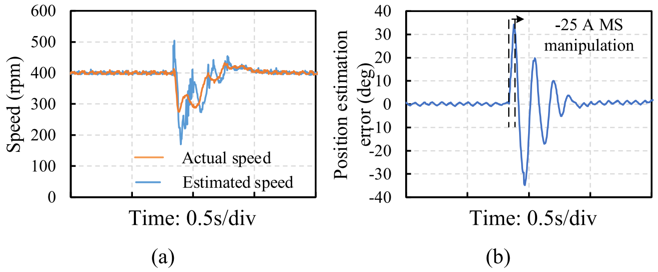

(a) (b)

Fig. 8. Experimental waveforms of speed and position estimation errors when conducting a -25 A MS manipulation under 0 N·m condition by using the conventional sensorless control based on SMO. (a) Actual and estimated speeds. (b) Position estimation error.

estimation performance of SMO cannot be maintained at all the cases when using the fixed parameters. Besides, the bandwidth of PLL also varies with back EMF. Therefore, for VFMM, the parameters of SMO and PLL should be prudently designed to achieve good performance under different conditions of speed and MS.

2) Position Estimation Error During MS Manipulation: For conventional PMSM, a relatively large position estimation error during acceleration or load change conditions is acceptable, although the performance is degraded correspondingly. However, for VFMM, a large position error may cause the actual MS deviates far from the preset MS, i.e., MS manipulation failure since a large *d*-axis current pulse will be applied during MS manipulation.

Fig. 7 shows the MS manipulations at the actual reference frame and the estimated reference frame. If there exists a position estimation error $\Delta\theta_e$, the real *d*-axis current can be expressed as follows:

$$i_d = \hat{i}_d \cos \Delta\theta_e \tag{11}$$

where $\hat{i}_d$ is the observed *d*-axis current under the estimated rotor position, and "cos(·)" is the cosine function.

In addition, a large position estimation error will aggravate the burden on the current controller to track its reference value. This makes the estimated current $\hat{i}_d$ deviate from its reference value $i_{d\mathrm{ref}}$, thus degrading the magnetization or demagnetization performance. Obviously, $\Delta\theta_e$ should be restricted to a certain range to guarantee the success of the MS manipulation.

3) Large Speed Fluctuation After MS Manipulation: Although the MS manipulation only lasts around 50 ms, a large speed fluctuation will occur and it requires relatively long time for the speed to recover to its steady value. As shown in Fig. 8, the actual speed measured by the encoder has an over 100 r/min variation when conducting a -25 A MS manipulation, which will seriously degrade the stability of the drive system. There are two main reasons for the speed fluctuation. First, the position estimation error resulted from the MS manipulation will cause mismatches in the torque production. Second, when the inaccurate speed estimation value is used as the feedback signal to generate the *dq*-axis reference currents, an unwanted torque oscillatory behavior will also occur.

4) Parameter Designs of Observers and PLL During MS Manipulation: As mentioned in Section III-C1, the parameters of observers and PLL should be well designed to ensure that the machine has good performance under different speed conditions for each certain choice of MS. However, even in that case, small position errors and low-speed fluctuations cannot be guaranteed during the short transition periods of MS manipulations. This greatly increases the difficulty in the parameter designs of sensorless control method for VFMM. It should be noted that this problem also exists when other sensorless control methods are employed.

IV. IMPROVED ADAPTIVE SMO-BASED SENSORLESS CONTROL

To overcome the above-mentioned difficulties, an improved adaptive SMO-based sensorless control strategy is proposed in this section in which the improvements are made from three aspects, i.e., more accurate VFMM model, higher performance SMO, and PLL.

A. Model Compensation for MS Manipulation

During an MS manipulation, the conventional SMO may cause large position error and speed fluctuation. In order to mitigate this impact, the *dq*-axis inductances are measured in advance by using an improved *dq*-axis voltage pulse injection method and updated into SMO, which can accelerate the convergence speed of the observer to reduce the position estimation error. The cross-saturation effect of the HMC-VFMM has been suppressed in the designing process and can be neglected subsequently. Therefore, it can be considered that the *dq*-axis inductances are only related to the *dq*-axis currents, respectively.

For the traditional PMSM, the *d*-axis flux can be calculated from

$$\psi_d = \int (u_d - Ri_d)dt = L_d(i_d)i_d + \psi_{\mathrm{PM}} \tag{12}$$

where ψ_{PM} is considered as a constant value and can be calculated from the no-load back EMF, and thus, $L_d(i_d)$ can be easily obtained. However, ψ_{PM} will change with i_d when applying a *d*-axis voltage pulse. The relationship between PM flux linkage and *d*-axis current, $\psi_{\mathrm{PM}}(i_d)$, as shown in Fig. 3, is utilized to address this problem. The schematic diagram of the proposed method is demonstrated in Fig. 9. First, due to the unknown MS of the machine, a -25 A i_d pulse is injected to demagnetize the machine to MS3, in step 1. Then, bipolar *d*-axis voltage sequence pulses are injected in step 2, and the *d*-axis flux linkage $\psi_d(i_d)$ can be determined by the recorded voltage $u_d(t)$ and current

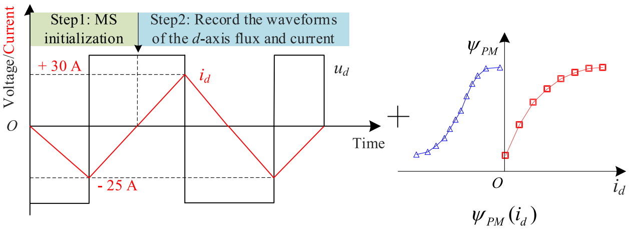

Fig. 9. Improved *dq*-axis voltage pulse injection method to measure the *d*-axis inductance.

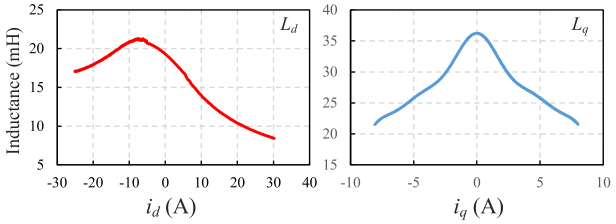

Fig. 10. Measured *dq*-axis inductances using improved *dq*-axis voltage pulse injection method.

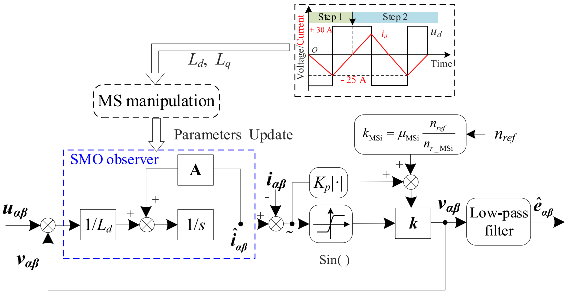

Fig. 11. Schematic diagram of the improved adaptive SMO.

$i_d(t)$ from (12). Therefore, the *d*-axis inductance $L_d(i_d)$ can be easily calculated with $\psi_{\mathrm{PM}}(i_d)$ and $\psi_d(i_d)$ based on (12). The *q*-axis inductance can be obtained similarly. It should be noted that for HMC-VFMM with negligible cross-saturation effect, it is unnecessary to adjust the initial MS when measuring *q*-axis inductance.

The measured *dq*-axis inductances are depicted in Fig. 10, which will be updated into the SMO to increase its convergence speed during MS manipulations and reduce the position estimation errors. Specifically, the *dq*-axis inductances can be fitted by using polynomial equations or stored as lookup tables for real-time invocation.

B. Improved Adaptive SMO

The schematic diagram of the improved adaptive SMO is shown in Fig. 11. It can be seen that the measured machine parameters during MS manipulations using the method in Section IV-A are updated into SMO as model compensation and an adaptive law is employed to tune the sliding-mode gain.

To mitigate the chattering problem when the discontinuous sign function is used, several switching functions, such as sigmoid function, supertwisting algorithm, hyperbolic tangent function, and sinusoidal function, are experimentally compared. Finally, the sinusoidal function, sin(·), is chosen to reduce the computational burden of the processor and maintain a satisfactory performance.

An adaptive algorithm considering both the MS and speed is proposed to tune the sliding-mode control gain k when the MS or speed changes. The control gains at the three MSs can be designed as follows:

$$k_{\mathrm{MS}i} = \mu_{\mathrm{MS}i}\frac{n_{\mathrm{ref}}}{n_{r\_\mathrm{MS}i}}, i = 1, 2, 3 \tag{13}$$

where $\mu_{\mathrm{MS}\,i}$ is the reference value of control gain at MSi and is selected based on the experimental results, n_{ref} is the reference speed, and n_{r_MSi} is the rated speed at MSi, which is chosen based on the corresponding speed operating range of MSi.

In addition, to increase the convergence speed during MS manipulation, the current observation error is used to further regulate the sliding-mode control gain as follows:

$$k = k_{\mathrm{MS}i} + K_p\left|\hat{i} - i\right| \tag{14}$$

where K_p is the proportional gain of current observation error, and i represents i_α or i_β.

The cutting frequency of the low-pass filter is designed to vary with speed so that the phase lag remains constant and is easy to be compensated. It should be noted that the SMO itself will also introduce a phase lag of extended EMF [27], besides low-pass filter. The phase lags at the three MSs should be measured through experiments and compensated correspondingly.

Then, the stability of the proposed adaptive SMO is analyzed to ensure the stable operation of the drive system. A Lyapunov function is constructed as follows:

$$V = \frac{1}{2}\left(\tilde{i}_\alpha^2 + \tilde{i}_\beta^2\right). \tag{15}$$

To make the system convergent, based on the theory of Lyapunov's stability, the derivative of the Lyapunov function [19] should satisfy the following condition:

$$\dot{V} = \tilde{i}_\alpha\frac{d\tilde{i}_\alpha}{dt} + \tilde{i}_\beta\frac{d\tilde{i}_\beta}{dt} \leq 0. \tag{16}$$

It is easy to obtain the $\alpha\beta$-axis current error equations of the proposed observer as follows:

$$\begin{cases} \frac{d\tilde{i}_\alpha}{dt} = -\frac{R}{L_d}\tilde{i}_\alpha - \hat{\omega}_e\frac{L_d-L_q}{L_d}\tilde{i}_\beta + \frac{1}{L_d}e_\alpha - \frac{1}{L_d}k\sin(\tilde{i}_\alpha) \\ \frac{d\tilde{i}_\beta}{dt} = -\frac{R}{L_d}\tilde{i}_\beta + \hat{\omega}_e\frac{L_d-L_q}{L_d}\tilde{i}_\alpha + \frac{1}{L_d}e_\beta - \frac{1}{L_d}k\sin(\tilde{i}_\beta). \end{cases} \tag{17}$$

By substituting (17) into (16), it can be obtained that

$$\begin{aligned} \dot{V} = & -\frac{R}{L_d}\tilde{i}_\alpha^2 - \hat{\omega}_e\frac{L_d - L_q}{L_d}\tilde{i}_\alpha\tilde{i}_\beta + \frac{1}{L_d}e_\alpha\tilde{i}_\alpha - \frac{1}{L_d}k\sin(\tilde{i}_\alpha)\tilde{i}_\alpha \\ & -\frac{R}{L_d}\tilde{i}_\beta^2 + \hat{\omega}_e\frac{L_d - L_q}{L_d}\tilde{i}_\alpha\tilde{i}_\beta + \frac{1}{L_d}e_\beta\tilde{i}_\beta - \frac{1}{L_d}k\sin(\tilde{i}_\beta)\tilde{i}_\beta \\ = & -\frac{R}{L_d}(\tilde{i}_\alpha^2 + \tilde{i}_\beta^2) + \frac{\tilde{i}_\alpha}{L_d}\left[e_\alpha - k\sin(\tilde{i}_\alpha)\right] + \frac{\tilde{i}_\beta}{L_d}\left[e_\beta - k\sin(\tilde{i}_\beta)\right] \\ = & V_1 + V_2 + V_3 \end{aligned} \tag{18}$$

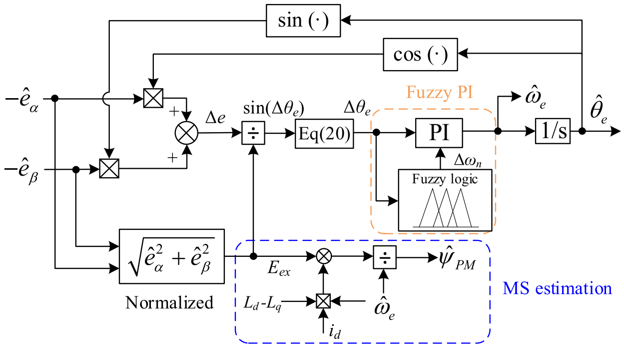

Fig. 12. Schematic diagram of the improved PLL.

TABLE I
FUZZY LOGIC OF $\Delta\omega_n$

$\Delta\dot{\theta}_e$	$\Delta\theta_e$						
	NB	NM	NS	ZO	PS	PM	PB
NB	NB	NB	NM	NM	NS	ZO	ZO
NM	NB	NB	NM	NS	NS	ZO	ZO
NS	NM	NM	NS	NS	ZO	PS	PS
ZO	NM	NM	NS	ZO	PS	PM	PM
PS	NM	NS	ZO	PS	PS	PM	PB
PM	ZO	ZO	PS	PS	PM	PB	PB
PB	ZO	ZO	PS	PM	PM	PB	PB

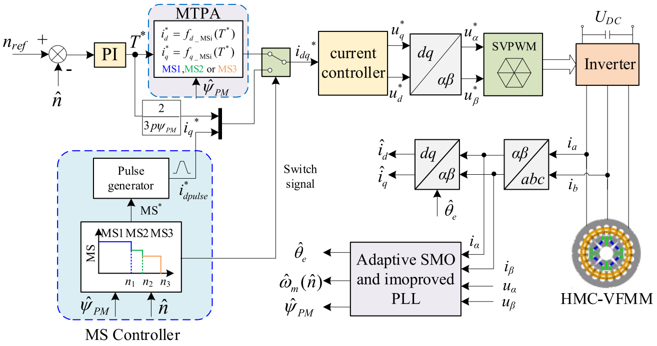

Fig. 13. Schematic diagram of the proposed sensorless control for VFMM.

where $V_1 = -\frac{R}{L_d}(\tilde{i}_\alpha^2 + \tilde{i}_\beta^2)$, $V_2 = \frac{\tilde{i}_\alpha}{L_d}[e_\alpha - k\sin(\tilde{i}_\alpha)]$, and $V_3 = \frac{\tilde{i}_\beta}{L_d}[e_\beta - k\sin(\tilde{i}_\beta)]$. Since $V_1 \leq 0$, the parameter k should be designed to ensure $V_2 \leq 0$ and $V_3 \leq 0$.

It is easy to know that when $k > |\frac{e_\alpha}{\sin(\tilde{i}_\alpha)}|$, $V_2 \leq 0$ is satisfied considering both $\tilde{i}_\alpha > 0$ and $\tilde{i}_\alpha < 0$. Similarly, when $k > |\frac{e_\beta}{\sin(\tilde{i}_\beta)}|$, $V_3 \leq 0$ is satisfied. Hence, when

$$k > \max\left(\left|\frac{e_\alpha}{\sin(\tilde{i}_\alpha)}\right|, \left|\frac{e_\beta}{\sin(\tilde{i}_\beta)}\right|\right). \tag{19}$$

$\dot{V} \leq 0$ can be guaranteed and the stability of the proposed improved adaptive SMO is proved.

C. Improved PLL

To increase the tracking ability, an improved PLL is proposed, as shown in Fig. 12, particularly for MS manipulations during which the position and speed estimation errors are relatively large. Commonly, when $|\Delta\theta_e| < \pi/6$, it can be assumed that $\sin(\Delta\theta_e) \approx \Delta\theta_e$, while a large $\Delta\theta_e$ will occur during MS manipulation. To enhance the position estimation performance, a third-order term is added to Taylor's formula when simplifying the position estimation error $\Delta\theta_e$, given by

$$\Delta\theta_e = \arcsin[\sin(\Delta\theta_e)] \approx \sin(\Delta\theta_e) + \frac{\sin{(\Delta\theta_e)}^3}{6}. \tag{20}$$

Second, the normalization of extended EMF is adopted in the PLL to keep the bandwidth constant considering the fact that the bandwidth variation of PLL system may deteriorate the tracking performance and increase the complexity of parameter design [24]. The transfer function of the PLL tracking observer can, thus, be further expressed as follows:

$$G_{\mathrm{PLL}} = \frac{\hat{\theta}_e}{\theta_e} = \frac{k_p s + k_i}{s^2 + k_p s + k_i}. \tag{21}$$

Commonly, the two PI gains are designed as follows:

$$k_p = 2\xi\omega_n, \quad k_i = \omega_n^2 \tag{22}$$

where ξ and ω_n are the damping and the bandwidth, respectively.

In addition, a fuzzy PI controller is employed to improve the dynamic performance of the PLL in which the input variables are the position estimation error ($\Delta\theta_e$) and its differential ($\Delta\dot{\theta}_e$), and the output variable is the bandwidth change of PLL ($\Delta\omega_n$), respectively. According to the fuzzy logic [30], [31], the output signal is quantized into seven levels represented by a set of linguistic variables: negative big (NB), negative medium (NM), negative small (NS), zero (ZO), positive small (PS), positive medium (PM), and positive big (PB). The fuzzy rules are described as follows:

1) When both the position error and its differential are large, $\Delta\omega_n$ should be increased a lot to improve the dynamic performance.
2) When the position error is relatively small and its differential is large, $\Delta\omega_n$ should be kept medium.
3) When both the position error and its differential are relatively small, $\Delta\omega_n$ should be appropriately decreased to suppress the influence of high frequency noise. The fuzzy rules of $\Delta\omega_n$ are formulated in Table I.

Besides, the PM flux linkage is online estimated through the MS estimation module by decoupling the extended EMF, as shown in Fig. 12. The estimated value will be utilized to determine the present MS and then used in the maximum-torque-per-ampere (MTPA) controller to allocate the *dq*-axis currents. In addition, the online estimated PM flux linkage will be used to detect the unintentional demagnetization. Once it occurs, an appropriate MS manipulation will be conducted to magnetize the machine to preset MS.

Fig. 13 demonstrates the schematic diagram of the improved adaptive SMO-based sensorless control strategy for VFMM. The extended EMFs are estimated through the adaptive SMO and the speed and position are obtained by using the improved PLL.

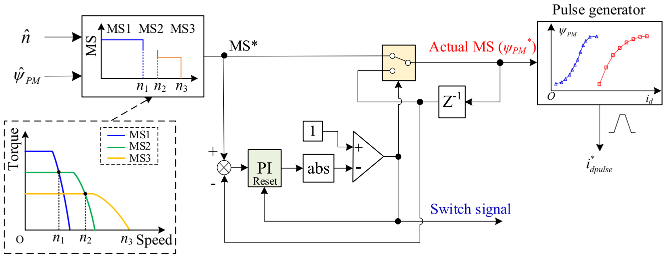

Fig. 14. Schematic diagram of the MS controller.

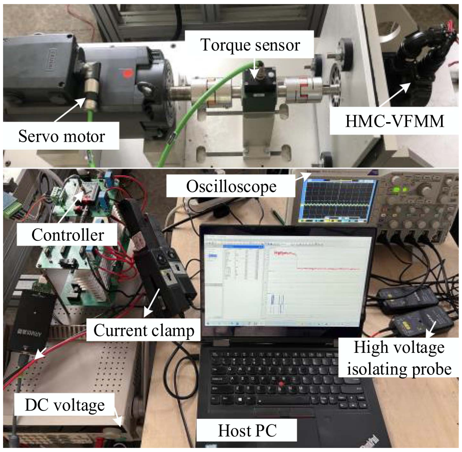

Fig. 15. Experimental setup.

In normal operation mode, the MTPA controller will generate the *dq*-axis reference currents according to the estimated MS and the torque command. Commonly, the relationships between the *dq*-axis currents and torque command at different MSs under MTPA control are measured in advance and embedded in controller for real-time invocation. In the MS manipulation, i_d current pulse $i^*_{d\text{pulse}}$ is generated by the MS controller and i_q command i^*_q is decoupled from the PM torque equation. The schematic diagram of the MS controller is shown in Fig. 14. The MS controller will determine the MS manipulations according to the switching speeds (n_1 and n_2), estimated MS and speed. A hysteresis controller [3] is adopted to reduce the frequency of MS manipulations when the machine runs around the switching speeds. Then, the pulse generator will generate the corresponding magnitudes of the required *d*-axis current pulses, during MS manipulations.

V. EXPERIMENTAL VALIDATION

The experimental setup used to validate the proposed control strategy is shown in Fig. 15. The HMC-VFMM under test is mechanically coupled with a torque meter and a servo motor. A three-phase half-bridge inverter consisting of six MOSFETS (FDA59N30) is used to feed the machine, and a microcontroller (STM32F407) is employed to implement the control strategy. An incremental encoder with 2500 lines is at the nondrive end of the machine to measure the real rotor position, which is only used for the postprocessing of position estimation error. The main parameters of the prototype are tabulated in Table II. The parameters of the conventional and proposed sensorless control strategies in the experiments are given in Table III.

TABLE II
MAIN PARAMETERS OF HMC-VFMM PROTOTYPE, DEFINITIONS OF DIFFERENT MSS, AND EXPERIMENTAL SETUP INFORMATION [2]

Symbol	Quantity	Value
U_{dc}	DC bus voltage	100 V
P_N	rated power	500 W
n_N	rated speed	800 r/min
p	pole pairs	2
I_N	rated current	7.5 A
ψ_{PM1}	PM flux linkage at MS1	0.263 Wb
ψ_{PM2}	PM flux linkage at MS2	0.210 Wb
ψ_{PM3}	PM flux linkage at MS3	0.152 Wb
R	phase resistance	1.3 Ω

TABLE III
PARAMETERS OF THE CONVENTIONAL SMO-BASED AND THE PROPOSED ADAPTIVE SMO-BASED SENSORLESS CONTROL STRATEGIES

Strategy	Parameters
Conventional SMO and PLL	$k = 100$, $k_p = 30$, $k_i = 2500$
Proposed adaptive SMO and PLL	$n_{r\_MS1} = 600$, $\mu_{MS1} = 200$, $n_{r\_MS2} = 800$, $\mu_{MS2} = 150$, $n_{r\_MS3} = 1000$, $\mu_{MS3} = 100$, $k_p = 30$, $k_i = 2500$

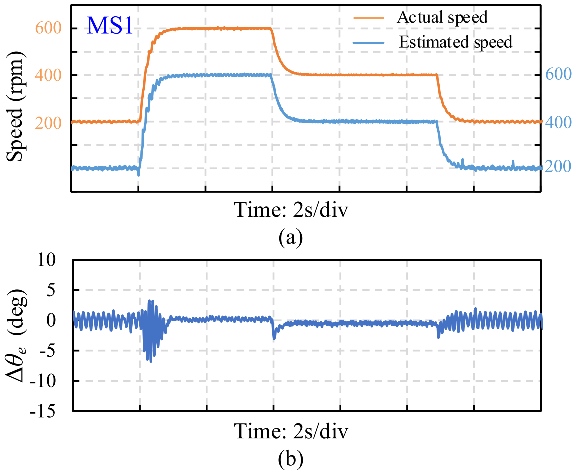

(a)

(b)

Fig. 16. Experimental results when the reference speed is changed from 200 to 600 to 400 to 200 r/min at MS1 by using the proposed strategy. (a) Speed. (b) Position estimation error.

A. Position Estimation Performance Under Different Conditions of MS and Speed

Figs. 16–18 show the experimental waveforms of actual speed, estimated speed, and position estimation error at the three MSs, respectively, where the speed is changed to demonstrate the position estimation performance of the proposed strategy. It can be found that the position estimation errors are quite small and the estimated speeds are very close to the actual ones under

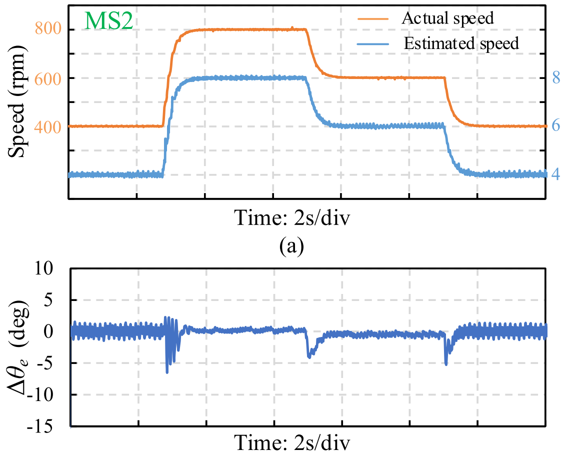

(a)

(b)

Fig. 17. Experimental results when the reference speed is changed from 400 to 800 to 600 to 400 r/min at MS2 by using the proposed strategy. (a) Speed. (b) Position estimation error.

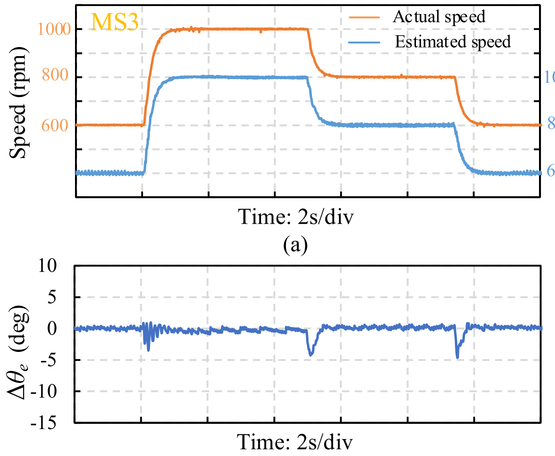

(a)

(b)

Fig. 18. Experimental results when the reference speed is changed from 600 to 1000 to 800 to 600 r/min at MS3 by using the proposed strategy. (a) Speed. (b) Position estimation error.

different conditions of speed and MS. The position estimation error is within 8° in the acceleration and deceleration processes, which is totally acceptable. By comparing the experimental results from the conventional and proposed strategies, as shown in Fig. 6 and Figs. 16 and 17, respectively, it can be seen that the position estimation accuracy under different conditions of MS, speed, and speed change has been significantly improved by employing the proposed strategy.

B. Position Estimation Performance During MS Manipulations

Figs. 19 and 22 demonstrate the experimental waveforms of actual speed, estimated speed, and position estimation error during four MS manipulations by using the conventional and proposed sensorless control strategies, respectively. The four MS manipulations are conducted successively by applying -15 A, -25 A, $+10$ A, and $+30$ A trapezoidal-shaped 52.5 ms d-axis current pulses at 400 r/min, respectively. The desired MS will be changed from MS1 to MS2, MS2 to MS3, MS3 to MS2, and MS2 to MS1, correspondingly. The peak–peak values of the position estimation errors and speed fluctuations during the four MS manipulations are listed in Table IV.

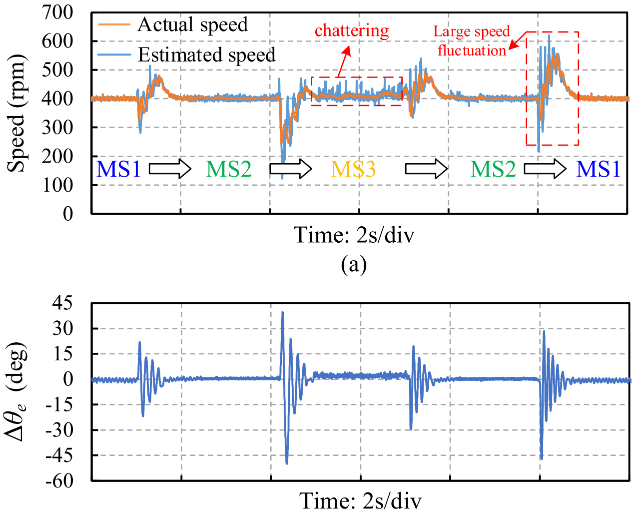

(a)

(b)

Fig. 19. Experimental results during the four MS manipulations by using the conventional sensorless control strategy. (a) Speed. (b) Position estimation error.

TABLE IV
PERFORMANCE COMPARISON DURING FOUR MS MANIPULATIONS

	Position estimation error (°)		Speed fluctuation (r/min)	
MS manipulation	Conventional strategy	Proposed strategy	Conventional strategy	Proposed strategy
–15 A	43.94	24.82	157.2	80.3
–25 A	89.71	34.41	192.9	113.5
+10 A	48.28	24.11	127.6	81.1
+30 A	74.37	23.57	227.2	57.6

When the conventional sensorless control is used, although the estimation errors of steady-state position and speed are very small at both MS1 and MS2, the speed chattering occurs at MS3 due to the reduced value of extended EMF. More severely, there are large position estimation errors and speed fluctuations during the MS manipulations. When conducting the -25 A MS manipulation, the position estimation error and actual speed fluctuation can reach up to 89.71° and 192.9 r/min (48.2% of the 400 r/min reference speed), respectively. By contrast, when adopting the proposed strategy, not only the speed variations at steady state become small and within 12.8 r/min (3.2% of the 400 r/min reference speed) at all the three MSs but also, during the four MS manipulations, the position estimation errors decrease by 43.5%, 61.6%, 50.1%, and 68.3%, respectively, and the speed fluctuations decrease by 48.9%, 41.2%, 36.4%, and 74.4%, respectively. In summary, the improved adaptive SMO-based sensorless control strategy can achieve considerable improvements in terms of position estimation performance and speed fluctuation mitigation.

Fig. 20 shows the $\alpha\beta$-axis current errors during the four MS manipulations using the conventional and proposed SMOs, respectively. It can be clearly seen that the current errors when

Conventional SMO and Conventional PLL

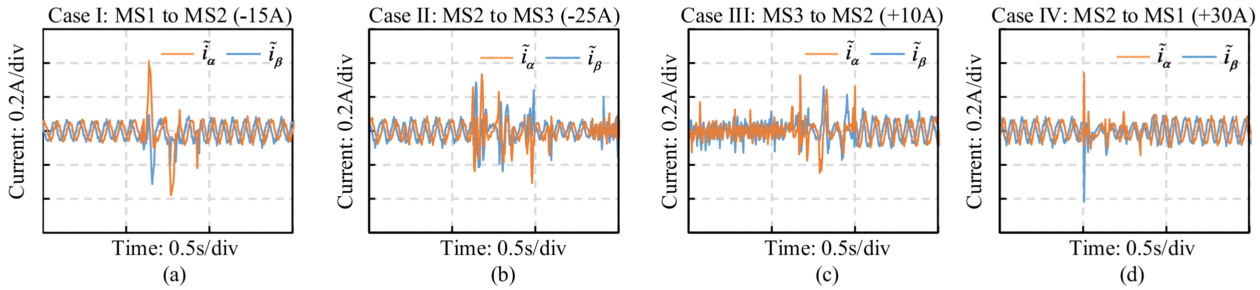

Proposed SMO and Conventional PLL

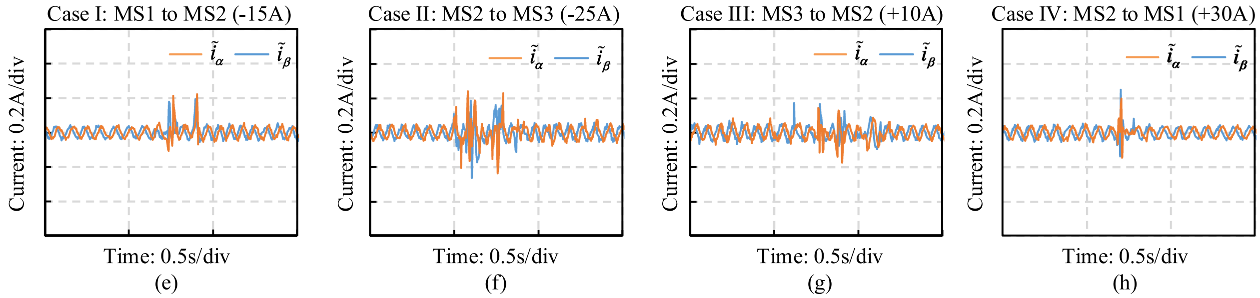

Fig. 20. $\alpha\beta$-axis current errors of SMO during the four MS manipulations using different methods. (a)–(d) Conventional SMO and conventional PLL. (e)–(h) Proposed SMO and conventional PLL.

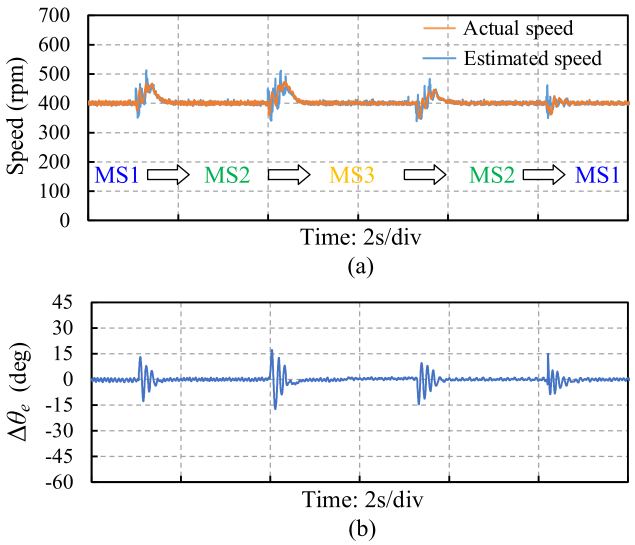

Fig. 22. Experimental results during the four MS manipulations by using the proposed sensorless control strategy. (a) Speed. (b) Position estimation error.

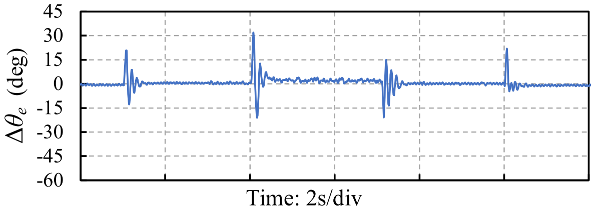

Fig. 21. Position estimation errors during the four MS manipulations using the conventional SMO and proposed improved PLL.

using the proposed SMO are much smaller than those when using the conventional SMO. It indicates that the proposed SMO has faster convergence speed and can estimate the extended EMFs more accurately, thereby validating its effectiveness.

Fig. 21 demonstrates the position estimation errors during the four MS manipulations using the conventional SMO and proposed PLL. Through comparing Fig. 19(b) with Fig. 21, it can be found that the proposed improved PLL has better tracking performance than the conventional PLL. It can also be found that the improved adaptive SMO can better estimate the extended EMFs by comparing Fig. 22(b)with Fig. 21 so that more accurate position estimation can be obtained. In conclusion, the effectiveness of the proposed adaptive SMO and the proposed PLL has been validated, respectively.

C. Magnetization and Demagnetization Performance

The line–line back EMF waveforms under the conventional and proposed sensorless control strategies are shown in Fig. 23(a)–(d), respectively, to compare the corresponding magnetization and demagnetization performance. The machine is at MS2 initially and then a +30 A *d*-axis current is applied to magnetize the machine to MS1. The line–line back EMF waveform at 200 r/min is subsequently measured and the PM flux linkage is calculated. Similarly, the line–line back EMF waveform after a −25 A MS manipulation is also measured. It can be seen that there are approximately 8.0% errors between the actual and the target PM flux linkages in the conventional strategy, resulting from the large position estimation errors during the MS manipulations. By contrast, the machine can be magnetized to the desired MSs with small errors (within 1.5%) by applying the proposed strategy, which can guarantee satisfactory magnetization and demagnetization performance.

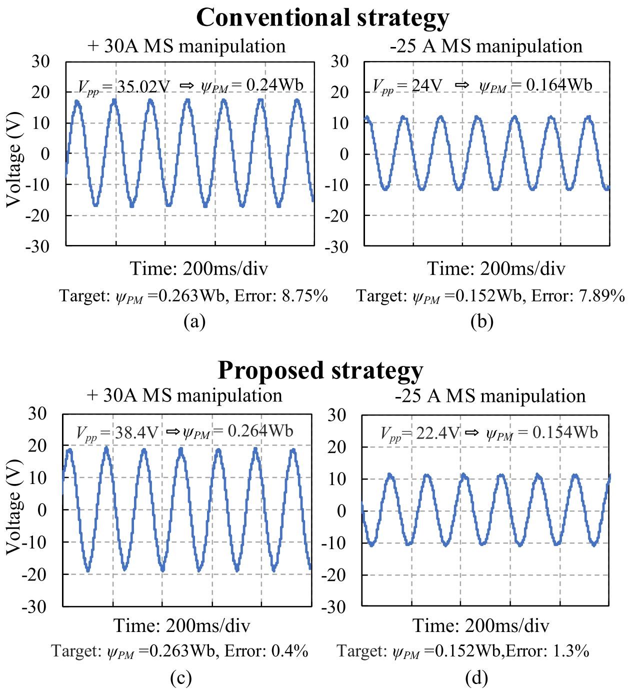

Target: ψ_{PM} =0.263Wb, Error: 8.75%
(a)

Target: ψ_{PM} =0.152Wb, Error: 7.89%
(b)

Target: ψ_{PM} =0.263Wb, Error: 0.4%
(c)

Target: ψ_{PM} =0.152Wb,Error: 1.3%
(d)

Fig. 23. Line–line back EMF waveforms at 200 r/min after a +30 A and a −25 A MS manipulations by using the conventional and proposed sensorless control strategies. (a) and (b) Conventional strategy. (c) and (d) Proposed strategy.

VI. CONCLUSION

This article investigates the position sensorless control for VFMM and proposes an improved adaptive SMO-based position sensorless control strategy to reduce the position estimation errors during MS manipulations. The major findings and contributions of this article can be summarized as follows.

1) The unique challenges of VFMM sensorless control are analyzed and summarized for the first time, including parameter designs of observer and PLL at different MSs and during MS manipulations, large position estimation error, and large speed fluctuation after MS manipulation.
2) The *dq*-axis inductances are measured by using a newly developed *dq*-axis voltage pulse injection method and updated into the improved adaptive SMO to enhance its tracking performance, particularly during MS manipulations.
3) The adaptive laws of sliding-mode gains are designed by considering the conditions of both MS and speed so that the machine can achieve small position estimation errors at different speeds and MSs, avoiding the chattering and instability problems.
4) An improved PLL is proposed and its PI gains are adaptively adjusted through fuzzy logic control, enhancing the dynamic performance.

In conclusion, the proposed sensorless control strategy for VFMM can achieve better position estimation accuracy at different MSs and speeds, particularly exhibiting satisfactory position estimation and speed fluctuation mitigation performance during MS manipulations, compared with the conventional strategy. The effectiveness of the proposed control strategy has been adequately verified by experiments on an HMC-VFMM.

Our future work will focus on the sensorless control of VFMMs under heavy-load conditions and investigate the performance of other advanced methods applied to VFMM sensorless control to seek the optimal one through comparing them with each other.

REFERENCES

[1] V. Ostovic, “Memory motors,” *IEEE Ind. Appl. Mag.*, vol. 9, no. 1, pp. 52–61, Jan./Feb. 2003.

[2] H. Yang, S. Lyu, H. Lin, Z.-Q. Zhu, H. Zhen, and T. Wang, “A novel hybrid-magnetic-circuit variable flux memory machine,” *IEEE Trans. Ind. Electron.*, vol. 67, no. 7, pp. 5258–5268, Jul. 2020.

[3] T. Fukushige, N. Limsuwan, T. Kato, K. Akatsu, and R. D. Lorenz, “Efficiency contours and loss minimization over a driving cycle of a variable flux-intensifying machine,” *IEEE Trans. Ind. Appl.*, vol. 51, no. 4, pp. 2984–2989, Jul./Aug. 2015.

[4] C.-Y. Yu, T. Fukushige, N. Limsuwan, T. Kato, D. D. Reigosa, and R. D. Lorenz, “Variable-flux machine torque estimation and pulsating torque mitigation during magnetization state manipulation,” *IEEE Trans. Ind. Appl.*, vol. 50, no. 5, pp. 3414–3422, Sep./Oct. 2014.

[5] Y. Zhong, H. Lin, J. Wang, Z. Chen, and H. Yang, “Speed fluctuation mitigation control for variable flux memory machine during magnetization state manipulations,” *IEEE Trans. Ind. Electron.*, vol. 70, no. 1, pp. 222–232, Jan. 2023.

[6] A. Athavale, D. J. Erato, and R. D. Lorenz, “Enabling driving cycle loss reduction in variable flux PMSMs via closed-loop magnetization state control,” *IEEE Trans. Ind. Appl.*, vol. 54, no. 4, pp. 3350–3359, Jul./Aug. 2018.

[7] Y. Zhong et al., “Variable time magnetization current trajectory control method for variable flux memory machine,” *IEEE Trans. Transp. Electrific.*, vol. 8, no. 3, pp. 3100–3110, Sep. 2022.

[8] J. Chen, J. Li, and R. Qu, “Analysis, modeling, and current trajectory control of magnetization state manipulation in variable-flux permanent magnet machines,” *IEEE Trans. Ind. Electron.*, vol. 66, no. 7, pp. 5133–5143, Jul. 2019.

[9] Y. Zhong, H. Lin, Z. Chen, S. Lyu, and H. Yang, “Online-parameter-estimation-based control strategy combining MTPA and flux-weakening for variable flux memory machines,” *IEEE Trans. Power Electron.*, vol. 37, no. 4, pp. 4080–4090, Apr. 2022.

[10] B. Basnet, A. M. Aljehaimi, and P. Pillay, “Back-EMF analysis of a variable flux machine for different magnetization states,” *IEEE Trans. Ind. Electron.*, vol. 68, no. 10, pp. 9125–9135, Oct. 2021.

[11] S. Lyu, H. Yang, H. Lin, H. Zhan, and Z. Chen, “Improved MTPA control for variable-flux memory machine with operating envelope prediction-based MS manipulation,” *IEEE Trans. Power Electron.*, vol. 38, no. 3, pp. 3700–3710, Mar. 2023.

[12] G. Wang, M. Valla, and J. Solsona, “Position sensorless permanent magnet synchronous machine drives—A review,” *IEEE Trans. Ind. Electron.*, vol. 67, no. 7, pp. 5830–5842, Jul. 2020.

[13] S. Morimoto, K. Kawamoto, M. Sanada, and Y. Takeda, “Sensorless control strategy for salient-pole PMSM based on extended EMF in rotating reference frame,” *IEEE Trans. Ind. Appl.*, vol. 38, no. 4, pp. 1054–1061, Jul./Aug. 2002.

[14] Q. Tang, A. Shen, X. Luo, and J. Xu, “PMSM sensorless control by injecting HF pulsating carrier signal into ABC frame,” *IEEE Trans. Power Electron.*, vol. 32, no. 5, pp. 3767–3776, May 2017.

[15] T. Zhang, Z. Xu, J. Li, H. Zhang, and C. Gerada, “A third-order super-twisting extended state observer for dynamic performance enhancement of sensorless IPMSM drives,” *IEEE Trans. Ind. Electron.*, vol. 67, no. 7, pp. 5948–5958, Jul. 2020.

[16] W. Xu, Y. Jiang, C. Mu, and F. Blaabjerg, “Improved nonlinear flux observer-based second-order SOIFO for PMSM sensorless control,” *IEEE Trans. Power Electron.*, vol. 34, no. 1, pp. 565–579, Jan. 2019.

[17] B. Yu et al., “A compensation strategy of flux linkage observer in SPMSM sensorless drives based on linear extended state observer,” *IEEE Trans. Energy Convers.*, vol. 37, no. 2, pp. 824–831, Jun. 2022.

[18] B. Hafez, A. S. Abdel-Khalik, A. M. Massoud, S. Ahmed, and R. D. Lorenz, “Single-sensor-based three-phase permanent-magnet synchronous motor drive system with Luenberger observers for motor line current reconstruction,” *IEEE Trans. Ind. Appl.*, vol. 50, no. 4, pp. 2602–2613, Jul./Aug. 2014.

[19] Z. Yin, Y. Zhang, X. Cao, D. Yuan, and J. Liu, “Estimated position error suppression using novel PLL for IPMSM sensorless drives based on full-order SMO,” *IEEE Trans. Power Electron.*, vol. 37, no. 4, pp. 4463–4474, Apr. 2022.

[20] M. Zhou, S. Cheng, Y. Feng, W. Xu, L. Wang, and W. Cai, “Full-order terminal sliding-mode-based sensorless control of induction motor with gain adaptation,” *IEEE J. Emerg. Sel. Topics Power Electron.*, vol. 10, no. 2, pp. 1978–1991, Apr. 2022.

[21] X. Sun, Y. Zhang, X. Tian, J. Cao, and J. Zhu, “Speed sensorless control for IPMSMs using a modified MRAS with gray wolf optimization algorithm,” *IEEE Trans. Transp. Electrific.*, vol. 8, no. 1, pp. 1326–1337, Mar. 2022.

[22] R. Dhaouadi, N. Mohan, and L. Norum, “Design and implementation of an extended Kalman filter for the state estimation of a permanent magnet synchronous motor,” *IEEE Trans. Power Electron.*, vol. 6, no. 3, pp. 491–497, Jun. 1991.

[23] D. Pasqualotto, S. Rigon, and M. Zigliotto, “Sensorless speed control of synchronous reluctance motor drives based on extended Kalman filter and neural magnetic model,” *IEEE Trans. Ind. Electron.*, vol. 70, no. 2, pp. 1321–1330, Feb. 2023.

[24] G. Zhang, G. Wang, D. Xu, and N. Zhao, “ADALINE-network-based PLL for position sensorless interior permanent magnet synchronous motor drives,” *IEEE Trans. Power Electron.*, vol. 31, no. 2, pp. 1450–1460, Feb. 2016.

[25] Z. Chen, A. A. Dawara, X. Zhang, H. Zhang, C. Liu, and G. Luo, “Adaptive sliding mode observer-based sensorless control for SPMSM employing a dual-PLL,” *IEEE Trans. Transp. Electrific.*, vol. 8, no. 1, pp. 1267–1277, Mar. 2022.

[26] W. Xu, S. Qu, J. Zhao, H. Zhang, and X. Du, “An improved full-order sliding-mode observer for rotor position and speed estimation of SPMSM,” *IEEE Access*, vol. 9, pp. 15099–15109, 2021.

[27] G. Liu, H. Zhang, and X. Song, “Position-estimation deviation-suppression technology of PMSM combining phase self-compensation SMO and feed-forward PLL,” *IEEE J. Emerg. Sel. Topics Power Electron.*, vol. 9, no. 1, pp. 335–344, Feb. 2021.

[28] S. Chen, X. Zhang, X. Wu, G. Tan, and X. Chen, “Sensorless control for IPMSM based on adaptive super-twisting sliding-mode observer and improved phase-locked loop,” *Energies*, vol. 12, no. 7, 2019, Art. no. 1225.

[29] D. Liang, J. Li, R. Qu, and W. Kong, “Adaptive second-order sliding-mode observer for PMSM sensorless control considering VSI nonlinearity,” *IEEE Trans. Power Electron.*, vol. 33, no. 10, pp. 8994–9004, Oct. 2018.

[30] L. Sheng, W. Li, Y. Wang, M. Fan, and X. Yang, “Sensorless control of a shearer short-range cutting interior permanent magnet synchronous motor based on a new sliding mode observer,” *IEEE Access*, vol. 5, pp. 18439–18450, 2017.

[31] C. Wang and Z. Q. Zhu, “Fuzzy logic speed control of permanent magnet synchronous machine and feedback voltage ripple reduction in flux-weakening operation region,” *IEEE Trans. Ind. Appl.*, vol. 56, no. 2, pp. 1505–1517, Mar./Apr. 2020.

[32] C. Wang, L. Gou, S. Dong, M. Zhou, and X. You, “Sensorless control of IPMSM based on super-twisting sliding mode observer with CVGI considering flying start,” *IEEE Trans. Transp. Electrific.*, vol. 8, no. 2, pp. 2106–2117, Jun. 2022.

[33] K. Liao, W. Xu, L. Bai, Y. Gong, M. M. Ismail, and I. Boldea, “Improved position sensorless piston stroke control method for linear oscillatory machine via an hybrid terminal sliding-mode observer,” *IEEE Trans. Power Electron.*, vol. 37, no. 12, pp. 14186–14197, Dec. 2022.

Yuxiang Zhong was born in Jiangsu Province, China, in 1998. He received the B.Eng. degree in electrical engineering from the Nanjing University of Astronautics and Aeronautics, Nanjing, China, in 2019. He is currently working toward the Ph.D. degree in electrical engineering with Southeast University, Nanjing, China.

His research interests include the control strategies of permanent magnet machines.

Heyun Lin (Senior Member, IEEE) received the B.S., M.S., and Ph.D. degrees in electrical engineering from the Nanjing University of Aeronautics and Astronautics, Nanjing, China, in 1985, 1989, and 1992, respectively.

From 1992 to 1994, he was a Postdoctoral Fellow with Southeast University, Nanjing, China. In 1994, he joined the School of Electrical Engineering, Southeast University, as an Associate Professor and has been a Full Professor since 2000. His main research is related to the design, analysis, and control of permanent magnet motor, intelligent electrical apparatus, and electromagnetic field numerical analysis. He is the author of more than 200 technical papers and the holder of 60 patents.

Dr. Lin is a Fellow of IET, a member of Electrical Motor and Apparatus Committee of Jiangsu Province, and a senior member of both China Society of Electrical Engineering and China Electrotechnical Society.

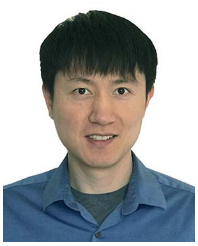

Jiyao Wang (Member, IEEE) received the B.S. degree from Tsinghua University, Beijing, China, and the Ph.D. degree from the University of Wisconsin-Madison, Madison, WI, USA, in 2010 and 2015, respectively, both in electrical engineering.

From 2016 to 2020, he was with Ford Motor Company, Dearborn, USA, where he was a part of the product development team for the electric motor control and drive system of Ford and Lincoln brand production level electric vehicles, including F150 Hybrid, Aviator Hybrid, and Mustang Mach-E. In 2021, he joined the Department of Electrical Engineering, Southeast University, Nanjing, China. His primary research interests include the designs and controls for the integration of electric machine drive system.

Hui Yang (Senior Member, IEEE) received the B.Eng. degree from the Dalian University of Technology, Dalian, China, in 2011, and the Ph.D. degree from Southeast University, Nanjing, China, in 2016, both in electrical engineering.

From 2014 to 2015, he was supported by the China Scholarship Council through a one-year joint Ph.D. studentship with The University of Sheffield, Sheffield, U.K. Since 2016, he has been with Southeast University, where he has been an Associate Professor with the School of Electrical Engineering. From 2019 to 2020, he served as a Postdoctoral Fellow with the School of Electrical Engineering, The Hong Kong Polytechnic University. He has authored or coauthored more than 70 IEEE Transactions papers, and served as a peer reviewer of more than 10 IEEE journals. His research interests include novel permanent-magnet machines and drives with particular reference to variable-flux machines for electric vehicles and renewable energy applications.

Dr. Yang was a recipient of Best Paper Awards in ICEMS 2014, EVER 2015, and ICEMS 2019, and the holder of 25 patents. He acts as an Editor for *World Electric Vehicle Journal*, a member of IEEE IES Electrical Machines Technical Committee, and IAS Electrical Machine Committee. He serves as a TPC-Track Chair of IEMDC 2021 as well as Session Chair in Intermag 2018, IEMDC 2019, ICEMS 2019, and IEMDC 2021. He is invited as a tutorial speaker of PESA 2020 and IEMDC 2021.